

Article

Mechanical Properties and Oxidation Behavior of Cr–Si–N Coatings

Li-Chun Chang ^{1,2}, Yu-Heng Liu ³ and Yung-I Chen ^{3,4,*}¹ Department of Materials Engineering, Ming Chi University of Technology, New Taipei 24301, Taiwan² Center for Plasma and Thin Film Technologies, Ming Chi University of Technology, New Taipei 24301, Taiwan³ Institute of Materials Engineering, National Taiwan Ocean University, Keelung 20224, Taiwan⁴ Center of Excellence for Ocean Engineering, National Taiwan Ocean University, Keelung 20224, Taiwan

* Correspondence: yichen@mail.ntou.edu.tw; Tel.: +886-2-2462-2192

Received: 28 July 2019; Accepted: 19 August 2019; Published: 20 August 2019



Abstract: Cr–Si–N coatings were prepared through reactive direct current magnetron sputtering using a high N₂/Ar flow ratio of 1. The addition of Si to improve the mechanical properties and oxidation resistance of Cr–N coatings was examined. The results indicated that the Cr–Si–N coatings with an Si content of <12 at % and an N content of >50 at % exhibited a cubic CrN phase with a columnar structure, whereas the coatings with 14 at % Si comprised of a nanocomposite structure, and the coatings with 16–18 at % Si were near-amorphous. The nanocomposite Cr₃₂Si₁₄N₅₄ coating possessed hardness and Young's modulus values of 17 and 209 GPa, respectively, accompanied with a hardness to effective Young's modulus (H/E^*) value of 0.077 and an elastic recovery (We) level of 55%—all the properties were highest within the as-deposited coating. The addition of Si was also beneficial to reduce the surface roughness and improve the oxidation resistance.

Keywords: Cr–Si–N; magnetron sputtering; mechanical properties; oxidation resistance

1. Introduction

Chromium nitride thin films have attracted widespread industrial applications [1] and academic studies because of their excellent mechanical properties [2,3], wear resistance [4,5], corrosion resistance [6], and oxidation resistance [7–10]. To meet the increasingly advanced industrial demands, ternary composite films have attracted researchers' attentions. Previous studies have demonstrated improved mechanical properties and oxidation resistance of chromium nitride by adding a third element, such as CrAlN [11,12], CrSiN [13], CrWN [14,15], and CrZrN [16]. CrSiN coatings have become a popular research topic [17–26], following the development of nanocomposite coatings and the pursuit of enhancing the mechanical properties. Nanocomposite nitride coatings (recognized as nc-Me_nN/a-Si₃N₄) [21,27,28] consist of transition-metal nitride nanocrystallinities surrounded by amorphous tissue. The main hardening mechanisms of Me–Si–N coatings were solid-solution strengthening and nanocomposite formation hardening [21,23], whereas the residual stress effect was next in importance [21]. Stoichiometric CrN coatings exhibited their lowest oxidation rate, up to 800 °C, caused by the lowest Cr₂O₃ growth rate on the surface [7], whereas stoichiometric CrN_x coatings included Cr and Cr₂N phases, promoting their oxidation rates. However, crystalline Cr₂O₃ oxides roughened the surface to a high level of 55.5–200 nm [7,29]. The increased oxidation resistance of Cr–Si–N coatings at 800 °C was attributed to the deficiency of grain boundaries in the original amorphous Si₃N₄ phase within the coatings and the formation of amorphous SiO₂, together with crystalline Cr₂O₃ on the coating surface [24,30]. The decomposition of CrN into Cr₂N and N₂ above 900 °C and subsequent oxidation restricted the oxidation resistance of Cr–Si–N coatings, and only

the coatings with certain Si contents exhibited excellent oxidation resistance up to 1000 °C [30]. Previous studies [2,31] reported that increasing the nitrogen gas flow rate supported the addition of N into the Cr matrix and produced various phases from Cr + Cr₂N to Cr₂N, Cr₂N + CrN, and CrN. In this study, Cr–Si–N coatings were prepared through magnetron cosputtering using a high N₂/Ar flow ratio of 1 to confirm the formation of the CrN phase. The goals of this work focused on the feasibility of introducing Si into Cr–N coatings to improve the mechanical properties and oxidation resistance. The oxidation resistance was evaluated at 600 °C in a 15 ppm O₂–N₂ atmosphere for 8 h and 16 h; this atmosphere and temperature provided realistic conditions for molding optical glass elements [32]. Also examined were the effects of Si addition on the structural variation, surface roughness, and residual stress of the annealed Cr–Si–N coatings.

2. Materials and Methods

Cr–Si–N coatings were prepared on silicon substrates and polished SUS420 stainless steel substrates through reactive direct current magnetron cosputtering. The samples prepared on the two kinds of substrate were fabricated in one batch. The sputtering equipment and processes were similar to those used for fabricating Hf–Si–N/Ti/Si assemblies, which were described in detail in a previous study [33]. Targets of 99.95% pure Cr and 99.999% Si with a diameter of 50.8 mm were adopted as source materials. The target to substrate distance was kept at 90 mm. The substrate holder was electrically grounded and rotated at a speed of 5 rpm without heating. Both the flow rates of Ar (99.99%) and N₂ (99.999%) were maintained at 10 sccm to maintain the working pressure at 0.4 Pa. Cr interlayers were deposited on the substrates to improve adhesion between the coatings and the substrates. Cr–Si–N coatings were deposited by applying a power of 100 W on the Cr target, whereas the Si target powers were set at 0, 25, 50, 75, 100, 125, and 150 W. A field emission electron probe microanalyzer (FE-EPMA, JXA-8500F, JEOL, Akishima, Japan) equipped with wavelength dispersive spectrometers was adopted to determine the chemical compositions of the coatings. The phases of the coatings were identified using a conventional X-ray diffractometer (XRD, X'Pert PRO MPD, PANalytical, Almelo, The Netherlands) with Cu K α radiation. The thickness of coatings was evaluated by field-emission scanning electron microscopy (FE-SEM, S4800, Hitachi, Tokyo, Japan). The nanostructure was examined using a transmission electron microscope (TEM, JEM-2010F, JEOL, Tokyo, Japan) equipped with energy dispersive spectroscopy (EDS, Inca x-sight, Oxford Instruments, Tokyo, Japan). The TEM samples were prepared by applying a focused ion beam system (FEI Nova 200, Hillsboro, OR, USA). A Pt layer was deposited to protect each free surface during sample preparation. The surface roughness values, Ra, of the coatings were evaluated using an atomic force microscope (AFM, Dimension 3100 SPM, NanoScope IIIa, Veeco, Santa Barbara, CA, USA). The hardness and Young's modulus values of the coatings were measured using a nanoindentation tester (TI-900 Triboindenter, Hysitron, Minneapolis, MN, USA) and calculated based on the Oliver and Pharr method [34]. The nanoindenter was equipped with a Berkovich diamond probe tip, which was 200 nm in diameter. The Poisson's ratio used was 0.24 for CrN [35]. The residual stress of the coatings was measured by the curvature method using Stoney's equation [33,36]. A scratch test (Scratch Tester, J & L Tech. Co., Gyeonggi-do, Korea), up to a maximum load of 50 N, was adopted to explore the adhesion properties of films on stainless steel substrates.

3. Results and Discussion

3.1. Chemical Compositions and Microstructure of As-Deposited Cr–Si–N Coatings

Table 1 shows the chemical compositions and deposition rates of the as-deposited CrN and Cr–Si–N coatings, prepared using various Si target powers. The oxygen contents in the as-deposited coatings were less than 5 at %. After ignoring the O content in these coatings, the N content was higher than 50 at % and the Si content varied from 0 to 18 at % with an increasing Si target power from 0 to 150 W, whereas the deposition rate increased from 5.9 to 9.8 nm/min, simultaneously. The thicknesses of the Cr₅₀N₅₀, Cr₄₃Si₅N₅₂, Cr₃₉Si₈N₅₃, Cr₃₅Si₁₂N₅₃, Cr₃₂Si₁₄N₅₄, Cr₂₉Si₁₆N₅₅, and Cr₂₉Si₁₈N₅₃ coatings were 739, 828,

853, 830, 769, 777, and 738 nm, respectively. An additional $\text{Cr}_{37}\text{Si}_{10}\text{N}_{53}$ coating, prepared following the process for $\text{Cr}_{39}\text{Si}_8\text{N}_{53}$ coatings on Ti interlayers, exhibited a chemical composition of 35.2 at % Cr, 9.4 at % Si, 50.4 at % N, 3.2 at % O, 1.8 at % Ti, and a thickness of 839 nm, which implied that the aforementioned chemical composition analysis for the as-deposited CrN and Cr–Si–N coatings affected by the Cr interlayer was limited.

Table 1. Chemical compositions, deposition rates, and surface roughness of as-deposited Cr–Si–N coatings.

Sample	Power (W)		Chemical Composition (at %)				D ¹ (nm/min)	Ra ² (nm)
	Cr	Si	Cr	Si	N	O		
$\text{Cr}_{50}\text{N}_{50}$	100	0	48.7 ± 0.4	–	49.3 ± 0.3	2.0 ± 0.2	5.9	6.2 ± 0.1
$\text{Cr}_{43}\text{Si}_5\text{N}_{52}$	100	25	42.1 ± 0.8	4.4 ± 0.1	50.5 ± 0.9	3.0 ± 0.3	6.6	6.8 ± 0.6
$\text{Cr}_{39}\text{Si}_8\text{N}_{53}$	100	50	37.7 ± 0.3	8.0 ± 0.1	50.7 ± 0.4	3.6 ± 0.1	7.8	2.4 ± 0.1
$\text{Cr}_{35}\text{Si}_{12}\text{N}_{53}$	100	75	33.7 ± 0.4	11.0 ± 0.1	50.7 ± 0.4	4.6 ± 0.3	8.3	2.7 ± 0.2
$\text{Cr}_{32}\text{Si}_{14}\text{N}_{54}$	100	100	30.0 ± 0.4	14.5 ± 0.1	51.5 ± 0.5	5.0 ± 0.1	8.1	2.3 ± 0.5
$\text{Cr}_{29}\text{Si}_{16}\text{N}_{55}$	100	125	28.1 ± 0.2	16.1 ± 0.1	53.7 ± 0.4	2.1 ± 0.2	8.9	0.9 ± 0.2
$\text{Cr}_{29}\text{Si}_{18}\text{N}_{53}$	100	150	28.4 ± 0.3	17.9 ± 0.1	51.3 ± 0.4	2.4 ± 0.1	9.8	0.9 ± 0.2

¹ D: Deposition rate. ² Ra: Surface roughness.

Figure 1 shows the XRD patterns of the as-deposited Cr–Si–N coatings. Because both the flow rates of Ar and N_2 were maintained at 10 sccm, forming a high flow ratio of the reactive gas to total gas, the deposited coatings with an Si content less than 12 at % exhibited a crystalline cubic phase of CrN without Cr or Cr_2N . The intensities and widths of the reflections of the $\text{Cr}_{32}\text{Si}_{14}\text{N}_{54}$ coatings were, respectively, lower and broader than those of the crystalline coatings, implying that the $\text{Cr}_{32}\text{Si}_{14}\text{N}_{54}$ coatings formed a nanocomposite structure, whereas further increasing the Si content to 16–18 at % resulted in a near-amorphous phase, also named an X-ray amorphous phase. The diffraction reflections of the crystalline Cr–Si–N coatings shifted toward higher two-theta angles with increasing Si content, which implied that the decrease in lattice constants was caused by substituting Si into the CrN lattice.

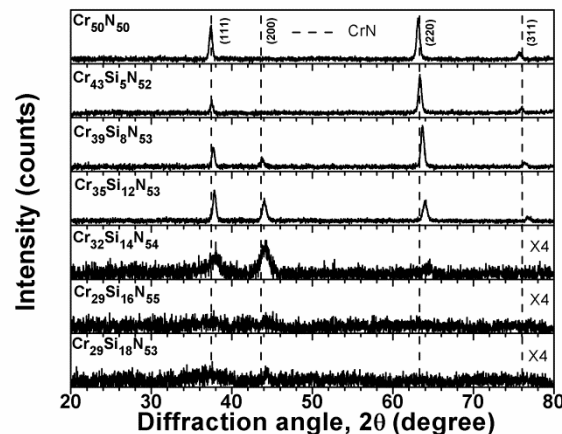


Figure 1. X-ray diffraction (XRD) patterns of as-deposited Cr–Si–N coatings (×4: multiplied by 4).

Figure 2 shows the lattice constants of the crystalline Cr–Si–N coatings determined using (111) and (220) reflections. The as-deposited $\text{Cr}_{50}\text{N}_{50}$ coatings exhibited lattice constants of 0.4158 and 0.4168 nm for (111) and (220) planes, respectively, which shrunk to 0.4140 nm after annealing at 600 °C in a 15 ppm O_2 – N_2 atmosphere for 16 h; the value of 0.4140 nm was identical to the standard value of a cubic CrN phase [ICDD 00-011-0065]. The expanded lattice of the as-deposited $\text{Cr}_{50}\text{N}_{50}$ coatings indicated the existence of interstitial Cr and N atoms. By contrast, the lattice constants of the CrN phase decreased with increasing Si content in the crystalline Cr–Si–N coatings, which implied that Si atoms (radius: 110 pm) substituted the Cr atoms (128 pm) in the CrN lattice structure [26]. Sandu et al. [21]

proposed a model regarding the film formation of sputtered M–Si–N coatings. The solubility limit of Si atoms in M–Si–N compounds was determined by examining the evolutions of crystalline grain sizes and lattice parameters as a function of Si addition. Si atoms segregated at the crystallite surfaces as the Si content exceeded the solubility limit, which resulted in the formation of a nanocomposite structure [21]. Benkahoul et al. [23], Martinez et al. [13], Lee and Chang [22], and Lin et al. [26] reported the solubility limit of Si atoms in Cr–Si–N coatings to be 2.3, 3, 4.1, and 4.8 at %, respectively. By contrast, the lattice constants decreased with increasing Si content up to 12 at % in this study, which suggested a high Si solubility. Park et al. [17] reported that the d-spacing of CrN (200) planes decreased with increasing Si content to 11.0 at %.

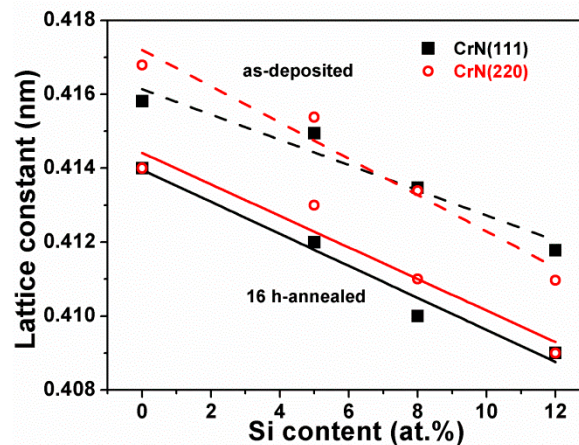


Figure 2. Lattice constants of the as-deposited and 16 h-annealed Cr–Si–N coatings determined from (111) and (220) reflections of the XRD patterns.

Figures 3–5 display the cross-sectional TEM images and selected-area diffraction patterns (SADPs) of the $\text{Cr}_{43}\text{Si}_5\text{N}_{52}$, $\text{Cr}_{32}\text{Si}_{14}\text{N}_{54}$, and $\text{Cr}_{29}\text{Si}_{18}\text{N}_{53}$ coatings, respectively. The $\text{Cr}_{43}\text{Si}_5\text{N}_{52}$ coating—a low Si content Cr–Si–N coating—exhibited an evident columnar structure growing through the entire coating (Figure 3a), with a width of 37–43 nm examined from the dark field image correlated with the diffraction spot of CrN (200) (Figure 3b). The $\text{Cr}_{32}\text{Si}_{14}\text{N}_{54}$ coating, a medium-Si-content coating, comprised of a dense structure with a ringed SADP (Figure 4a). Figure 4b shows that the $\text{Cr}_{32}\text{Si}_{14}\text{N}_{54}$ coating consisted of nanoscale crystals with a width of 10 nm and a length of 32 nm, implying the formation of a nanocomposite structure. The $\text{Cr}_{29}\text{Si}_{18}\text{N}_{53}$ coating, a high-Si-content coating, exhibited diffused ring patterns (Figure 5a), for which the dark field image displayed lots of randomly distributed spots (Figure 5b). Moreover, the high-resolution image exhibited short-range crystalline domains with a diameter of approximately 2 nm (Figure 5c); therefore, the $\text{Cr}_{29}\text{Si}_{18}\text{N}_{53}$ coating was near-amorphous. The structure of Cr–Si–N coatings varied from crystalline columnar, to nanocomposite, and then to a near-amorphous structure with increasing Si content. Table 1 lists the surface roughness values of the Cr–Si–N coatings. The crystalline $\text{Cr}_{50}\text{N}_{50}$ and $\text{Cr}_{43}\text{Si}_5\text{N}_{52}$ coatings with low Si contents exhibited a high surface roughness of 6.2–6.8 nm, whereas the $\text{Cr}_{39}\text{Si}_8\text{N}_{53}$, $\text{Cr}_{35}\text{Si}_{12}\text{N}_{53}$, and $\text{Cr}_{32}\text{Si}_{14}\text{N}_{54}$ coatings with medium Si contents exhibited a medium surface roughness of 2.3–2.7 nm, and the $\text{Cr}_{29}\text{Si}_{16}\text{N}_{55}$ and $\text{Cr}_{29}\text{Si}_{18}\text{N}_{53}$ coatings with high Si contents exhibited a low surface roughness of 0.9 nm. The surface roughness of the Cr–Si–N coatings exhibited decreased upon increasing Si content, accompanied with a decrease in crystalline dimensions.

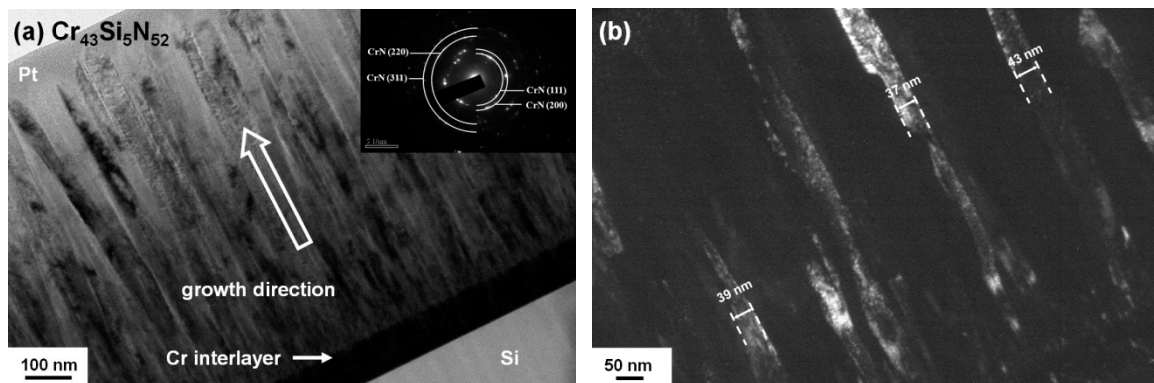


Figure 3. (a) Cross-sectional transmission electron microscope (TEM) image and selected-area diffraction pattern (SADP; inset) of the $\text{Cr}_{43}\text{Si}_5\text{N}_{52}$ coating; (b) the dark field image correlated with the diffraction spot of CrN (200) in the SADP.

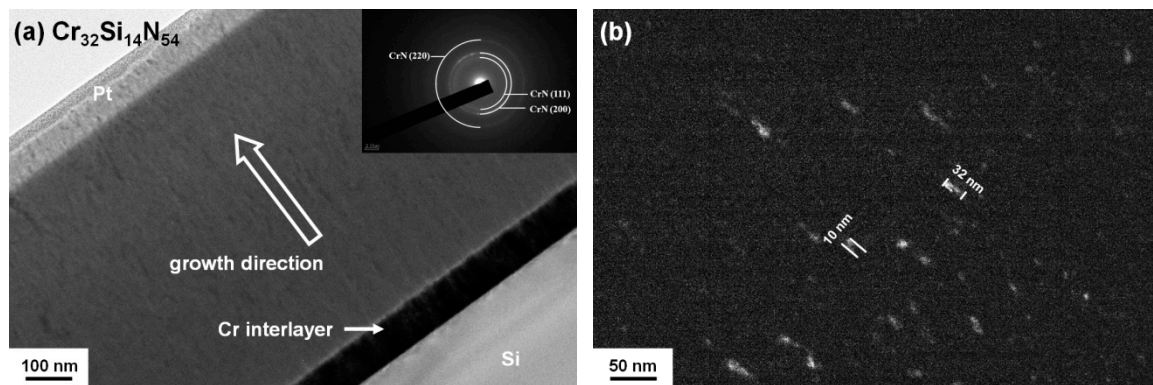


Figure 4. (a) Cross-sectional TEM image and selected-area diffraction pattern (SADP) of the $\text{Cr}_{32}\text{Si}_{14}\text{N}_{54}$ coating; (b) the dark field image correlated with the diffraction ring of CrN (200) in the SADP.

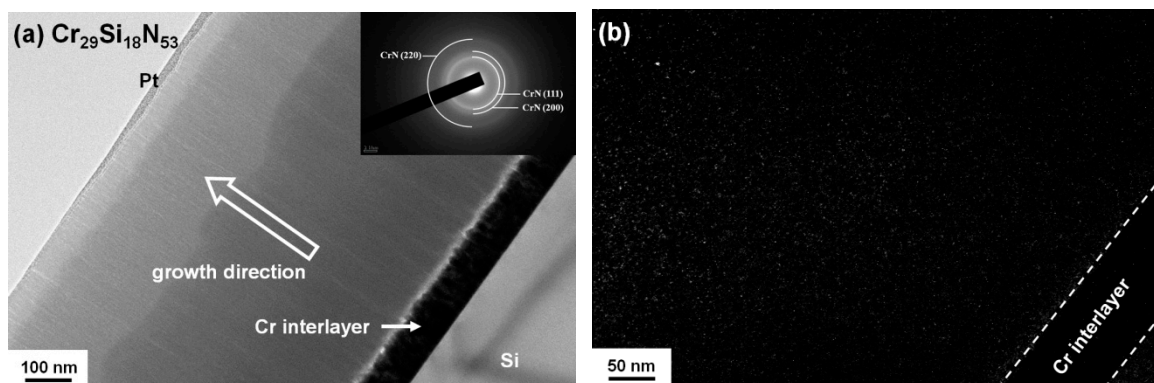


Figure 5. Cont.

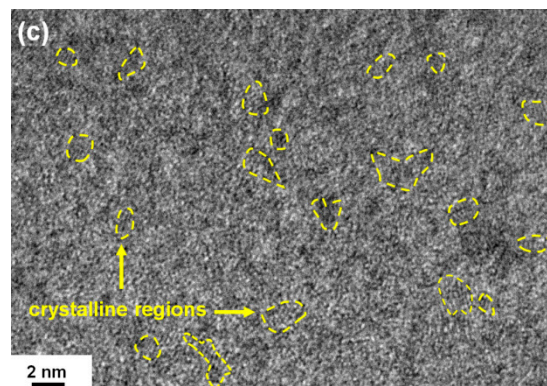


Figure 5. (a) Cross-sectional TEM image and selected-area diffraction pattern (SADP) of the $\text{Cr}_{29}\text{Si}_{18}\text{N}_{53}$ coating; (b) the dark field image correlated with the diffraction spot of CrN (111) in the SADP; (c) parts of the crystalline regions in the high-resolution TEM image (highlighted by yellow dashed lines).

3.2. Mechanical Properties of As-Deposited Cr–Si–N Coatings

The $\text{Cr}_{50}\text{N}_{50}$ coating exhibited hardness and Young's modulus values of 5.9 and 154 GPa (Table 2), respectively. The fact that the mechanical properties exhibited low levels should be attributed to the sputtering process having been performed without applying bias voltage and heating the substrates, which resulted in a loosely packed structure with the existence of interstitial Cr and N atoms. Previous works have reported hardness levels of 18–21 GPa for CrN coatings [2,4,11,15,19,37–39]. Lee et al. [37] reported a hardness of 9.6 GPa for CrN coatings prepared through pulsed direct current reactive magnetron sputtering without applying substrate bias and heated temperature; moreover, a CrN film with a hardness of 21 GPa was deposited at -290 V bias and 300 °C. Figure 6 illustrates the hardness and Young's modulus values of Cr–Si–N coatings with various Si contents. The hardness and Young's modulus values of the Cr–Si–N coatings initially increased with increasing Si content, reached maximum levels for the $\text{Cr}_{32}\text{Si}_{14}\text{N}_{54}$ coating, and then decreased with the further addition of Si. The $\text{Cr}_{32}\text{Si}_{14}\text{N}_{54}$ coating exhibited the highest hardness and Young's modulus levels of 17 GPa and 209 GPa, respectively. Because all the as-deposited Cr–Si–N coatings exhibited a low residual stress of 0.2–0.9 GPa in tension, the hardness enhancement was attributed to the formation of solid solutions and nanocomposite structures. The decline in hardness of the coatings with a high Si content was attributed to the high volume of amorphous Si_3N_4 . Musil [40] proposed that hard nanocomposite coatings with enhanced toughness should exceed the criteria of $H/E^* > 0.1$ and $We \geq 60\%$, where E^* is the effective Young's modulus and We is the elastic recovery. The four crystalline Cr–Si–N coatings exhibited low H/E^* values of 0.035–0.043 and We levels in the range of 34%–40%. The nanocomposite $\text{Cr}_{32}\text{Si}_{14}\text{N}_{54}$ coating exhibited an H/E^* value of 0.077 and a We level of 55%, which were the highest levels among the as-deposited coatings. The near-amorphous $\text{Cr}_{29}\text{Si}_{16}\text{N}_{55}$ and $\text{Cr}_{29}\text{Si}_{18}\text{N}_{53}$ coatings exhibited H/E^* values of 0.066–0.069 and We levels of 50%–53%.

Table 2. Mechanical properties and residual stresses of as-deposited Cr–Si–N coatings.

Sample	H^1 (GPa)	E^2 (GPa)	H/E^*	We^3 %	Stress (GPa)
$\text{Cr}_{50}\text{N}_{50}$	5.9 ± 0.3	154 ± 8	0.036	37	0.4 ± 0.1
$\text{Cr}_{43}\text{Si}_5\text{N}_{52}$	5.5 ± 0.6	148 ± 6	0.035	35	0.2 ± 0.1
$\text{Cr}_{39}\text{Si}_8\text{N}_{53}$	6.1 ± 0.3	154 ± 13	0.037	34	0.4 ± 0.1
$\text{Cr}_{35}\text{Si}_{12}\text{N}_{53}$	7.5 ± 0.6	164 ± 7	0.043	40	0.5 ± 0.1
$\text{Cr}_{32}\text{Si}_{14}\text{N}_{54}$	17.0 ± 0.6	209 ± 3	0.077	55	0.7 ± 0.1
$\text{Cr}_{29}\text{Si}_{16}\text{N}_{55}$	14.3 ± 0.7	203 ± 6	0.066	50	0.9 ± 0.2
$\text{Cr}_{29}\text{Si}_{18}\text{N}_{53}$	14.2 ± 0.7	195 ± 5	0.069	53	0.6 ± 0.1

¹ H : Hardness. ² E : Young's modulus. ³ We : Elastic recovery.

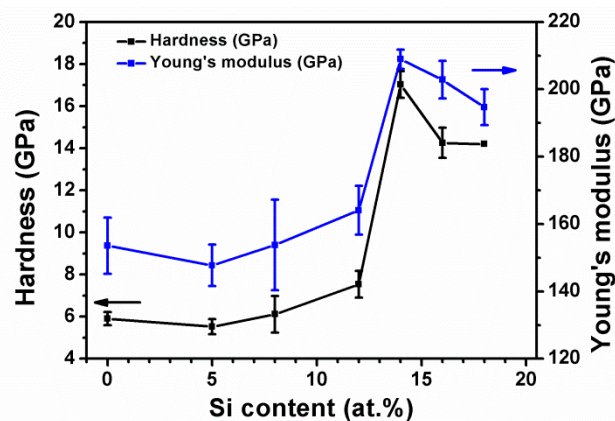


Figure 6. Hardness and Young's modulus values of Cr-Si-N coatings with different silicon contents.

Figure 7 presents optical micrographs of the scratch tracks of Cr-Si-N coatings with various Si contents prepared on stainless steel substrates. The critical loads L_{c1} and L_{c2} were defined as the loads inducing the first cohesive failure and the first exposure of the substrate material, respectively [41]. The L_{c1} and L_{c2} values of the Cr-Si-N coatings with an Si content less than 12 at % remained at 13.1–13.9 N and 21.6–24.5 N, respectively. The L_{c1} and L_{c2} values decreased abruptly as the phase structure was altered from crystalline to nanocomposite. The nanocomposite and near-amorphous Cr-Si-N coatings exhibited L_{c1} and L_{c2} levels of 7.1–8.1 N and 15.7–16.7 N, respectively. Scratch tests indicated that the adhesion strength was related to the coatings' phase structures.



Figure 7. Optical micrograph of the scratch tracks of Cr-Si-N coatings with various Si contents prepared on stainless steel substrates.

3.3. Oxidation Behavior of Cr-Si-N Coatings

Figure 8a shows the XRD patterns of the Cr-Si-N coatings annealed in 15 ppm O_2-N_2 at 600 °C for 8 h. Cr_2O_3 reflections were observed for the crystalline $Cr_{50}N_{50}$, $Cr_{43}Si_5N_{52}$, $Cr_{39}Si_8N_{53}$, and $Cr_{35}Si_{12}N_{53}$ coatings, whereas the nanocomposite $Cr_{32}Si_{14}N_{54}$ and near-amorphous $Cr_{29}Si_{16}N_{55}$ and $Cr_{29}Si_{18}N_{53}$ coatings maintained patterns similar to those of samples in the as-deposited state. Figure 8b shows the XRD patterns of the 16 h-annealed samples, which were similar to those of the 8 h-annealed samples. Figure 2 shows the lattice constants of the as-deposited and 16 h-annealed crystalline Cr-Si-N coatings and

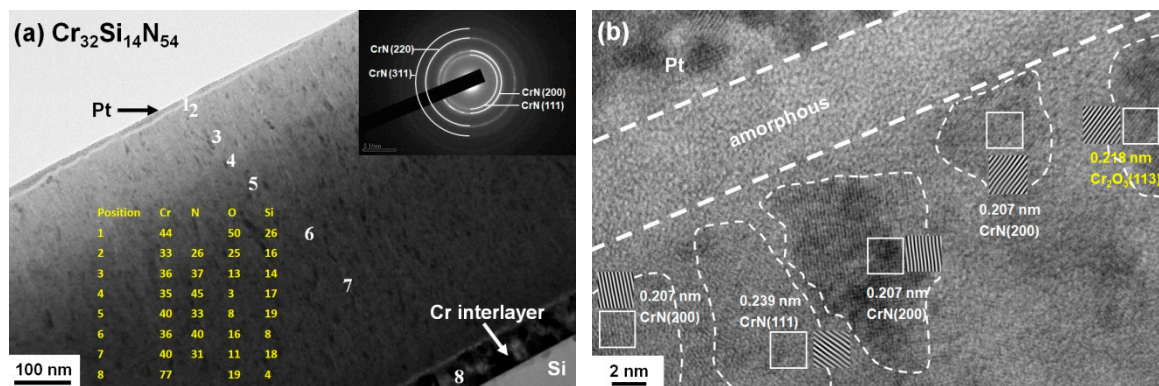


Figure 10. (a) Cross-sectional TEM image, selected-area diffraction pattern (inset), and EDS results (given in yellow) of the $\text{Cr}_{32}\text{Si}_{14}\text{N}_{54}$ coating after annealing in 15 ppm $\text{O}_2\text{-N}_2$ at 600 °C for 16 h; (b) the high-resolution TEM image.

Figure 11a displays a cross-sectional TEM image of a 16 h-annealed $\text{Cr}_{29}\text{Si}_{18}\text{N}_{53}$ sample. The structure was dense without evident grain boundaries. The SADP exhibited diffused ring patterns sharper than those shown in the as-deposited state (Figure 5a), which indicated that the crystallinity was enhanced after annealing at 600 °C. The SADP further indicated that the main crystalline species was CrN. Figure 11b shows a high-resolution TEM image at the near-surface region, which exhibits an amorphous oxide scale of approximately 4 nm in thickness. Beneath the surface oxide scale, discrete CrN and Cr_2O_3 crystalline domains were dispersed in an amorphous matrix.

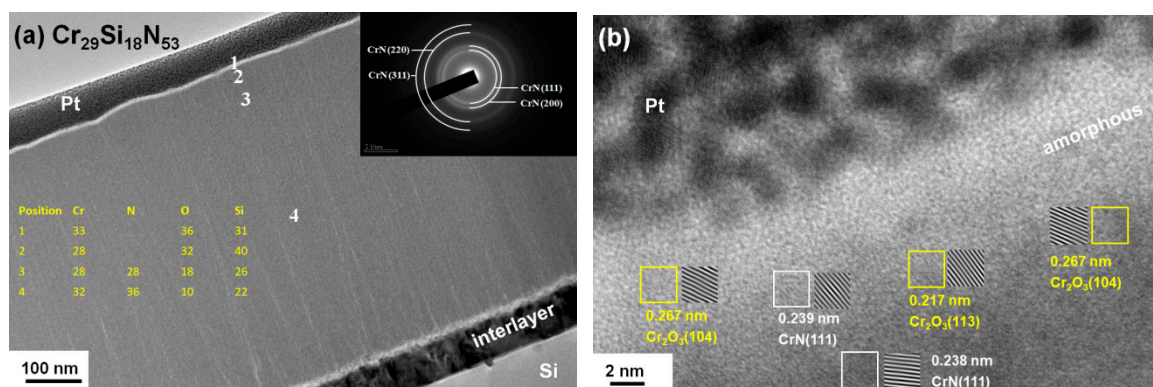


Figure 11. (a) Cross-sectional TEM image, selected-area diffraction pattern (inset), and EDS results (shown in yellow) of the $\text{Cr}_{29}\text{Si}_{18}\text{N}_{53}$ coating after annealing in 15 ppm $\text{O}_2\text{-N}_2$ at 600 °C for 16 h; (b) the high-resolution TEM image.

Table 3 shows the chemical compositions of the as-deposited and annealed crystalline $\text{Cr}_{50}\text{N}_{50}$, nanocomposite $\text{Cr}_{32}\text{Si}_{14}\text{N}_{54}$, and near-amorphous $\text{Cr}_{29}\text{Si}_{18}\text{N}_{53}$ coatings. The O content of the $\text{Cr}_{50}\text{N}_{50}$ coating increased from 2.0 to 30.6 and 29.9 at % as the annealing time was increased from 0 to 8 and 16 h, respectively. The 8 and 16 h-annealed $\text{Cr}_{50}\text{N}_{50}$ coatings maintained a high surface roughness level of 5 nm, an increased tensile residual stress of 1 GPa, an increased hardness level of 19.7–20.8 GPa, and an enhanced Young's modulus in the range of 197–247 GPa. The O content of the $\text{Cr}_{32}\text{Si}_{14}\text{N}_{54}$ coating increased from 5 to 10 at % after annealing for 8–16 h, whereas the surface roughness remained at 2.6–2.7 nm, the residual stress increased from 0.7 to 1.3–2.4 GPa, the hardness increased to 20.0–22.4 GPa, and the Young's modulus increased to 261–268 GPa. The O content of the $\text{Cr}_{29}\text{Si}_{18}\text{N}_{53}$ coating increased from 2.4 to 3.2–4.6 at % after annealing for 8–16 h, whereas the surface roughness increased from 0.9 to 1.9–2.6 nm, the residual stress increased from 0.6 to 1.4 GPa, the hardness increased to 20.0 GPa, and the Young's modulus increased to 251–254 GPa. The hardness levels of all the above three annealed coatings increased to 19.7–22.4 GPa, whereas the H/E^* ratio increased to a high range of 0.070–0.094

(Figure 12). The improvement in the mechanical properties of the annealed $\text{Cr}_{50}\text{N}_{50}$ coatings was accompanied by the recovery of the expanded lattice. Moreover, the reported hardness values of CrN , Cr_2O_3 , and SiO_2 films were 18–21, 29–32 [42–44], and 8–11 [45] GPa, respectively. Therefore, the annealed Cr–Si–N coatings exhibited a hardness level of 20–22 GPa. In summary, the Cr–Si–N coatings with an Si content >14 at % exhibited oxidation resistance in 15 ppm $\text{O}_2\text{-N}_2$ at 600 °C for 16 h.

Table 3. Chemical compositions, surface roughness, residual stresses, and mechanical properties of Cr–Si–N coatings annealed in 15 ppm $\text{O}_2\text{-N}_2$ at 600 °C.

Sample	Time ¹ (h)	Chemical Composition (at %)				Ra ² (nm)	Stress (GPa)	H ³ (GPa)	E ⁴ (GPa)	H/E*
		Cr	Si	N	O					
$\text{Cr}_{50}\text{N}_{50}$	0	48.7 ± 0.4	–	49.3 ± 0.3	2.0 ± 0.2	6.2 ± 0.1	0.4 ± 0.1	5.9 ± 0.3	154 ± 8	0.036
	8	42.9 ± 0.2	–	26.3 ± 0.5	30.8 ± 0.6	4.7 ± 0.1	1.1 ± 0.0	19.7 ± 1.4	197 ± 6	0.094
	16	42.4 ± 0.2	–	27.7 ± 0.2	29.9 ± 0.1	5.3 ± 0.1	1.0 ± 0.0	20.8 ± 1.4	247 ± 9	0.079
$\text{Cr}_{32}\text{Si}_{14}\text{N}_{54}$	0	30.0 ± 0.4	14.5 ± 0.1	51.5 ± 0.5	5.0 ± 0.1	2.3 ± 0.5	0.7 ± 0.1	17.0 ± 0.6	209 ± 3	0.077
	8	29.4 ± 0.2	13.1 ± 0.1	47.6 ± 0.2	9.9 ± 0.3	2.6 ± 0.1	1.3 ± 0.0	22.4 ± 1.0	261 ± 14	0.081
	16	30.8 ± 0.3	13.6 ± 0.1	45.5 ± 0.4	10.1 ± 0.0	2.7 ± 0.0	2.4 ± 0.1	20.0 ± 1.4	268 ± 12	0.070
$\text{Cr}_{29}\text{Si}_{18}\text{N}_{53}$	0	28.4 ± 0.3	17.9 ± 0.1	51.3 ± 0.4	2.4 ± 0.1	0.9 ± 0.2	0.6 ± 0.1	14.2 ± 0.7	195 ± 5	0.069
	8	27.8 ± 0.1	17.3 ± 0.1	50.3 ± 0.3	4.6 ± 0.2	1.9 ± 0.1	1.4 ± 0.0	20.0 ± 1.7	254 ± 15	0.074
	16	27.4 ± 0.4	17.2 ± 0.3	52.2 ± 0.4	3.2 ± 0.1	2.6 ± 0.0	1.4 ± 0.3	20.0 ± 1.0	251 ± 10	0.075

¹ Time: Annealing time. ² Ra: Surface roughness. ³ H: Hardness. ⁴ E: Young's modulus.

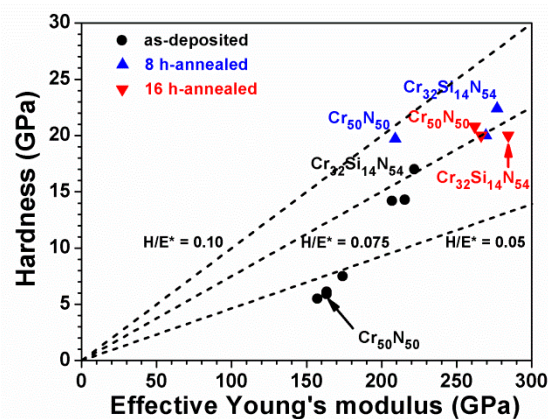


Figure 12. Relationship between hardness and effective Young's modulus of the as-deposited and annealed Cr–Si–N coatings.

4. Conclusions

This study presents the fabrication of Cr–Si–N coatings through reactive direct current magnetron cosputtering. The Si content of Cr–Si–N coatings ranged from 0 to 18 at % and was controlled by varying the sputter power applied to the Si target, whereas the N content remained higher than 50 at %, which was attributed to a high N_2/Ar flow ratio of 1. The mechanical properties of the Cr–Si–N coatings initially increased with increasing Si content, accompanied with the formation of a cubic CrN phase, reached maximum levels for the nanocomposite $\text{Cr}_{32}\text{Si}_{14}\text{N}_{54}$ coating, and then decreased with further addition of Si accompanied with the formation of a near-amorphous phase. The addition of Si was also beneficial to reduce the surface roughness. The roughness level of the near-amorphous coatings with a Si content >16 at % was less than 1 nm.

The addition of >14 at % Si content into Cr–N coatings increased the oxidation resistance in 15 ppm $\text{O}_2\text{-N}_2$ at 600 °C for up to 16 h of annealing by forming an amorphous oxide scale on the free surface, accompanied with a surface roughness of 2.6–2.7 nm. The improvement in the mechanical properties of the annealed Cr–Si–N coatings was attributed to the recovery of the expanded lattice and the high mechanical properties of Cr_2O_3 . Further research should focus on the effects of substrate bias and temperature on improving the characteristics of Cr–Si–N films.

Author Contributions: Conceptualization, L.C.C. and Y.I.C.; Funding acquisition, L.C.C. and Y.I.C.; Investigation, Y.H.L.; Project administration, Y.I.C.; Resources, L.C.C. and Y.I.C.; Validation, L.C.C.; Writing—original draft, Y.I.C.

Funding: This research was funded by the Ministry of Science and Technology, Taiwan, grant numbers 105-2221-E-019-007-MY3 and 107-2221-E-131-004. The APC was funded by National Taiwan Ocean University.

Acknowledgments: The authors thank Mei-Chen Chiang at Ming Chi University of Technology for technical support with TEM observations.

Conflicts of Interest: The authors declare no conflict of interest. The funders had no role in the design of the study; in the collection, analyses, or interpretation of data; in the writing of the manuscript, or in the decision to publish the results.

References

1. Navinšek, B.; Panjan, P.; Mološev, I. Industrial applications of CrN (PVD) coatings, deposited at high and low temperatures. *Surf. Coat. Technol.* **1997**, *97*, 182–191. [[CrossRef](#)]
2. Hones, P.; Sanjines, R.; Lévy, F. Characterization of sputter-deposited chromium nitride thin films for hard coatings. *Surf. Coat. Technol.* **1997**, *94–95*, 398–402. [[CrossRef](#)]
3. Mayrhofer, P.H.; Mitterer, C.; Musil, J. Structure–property relationships in single- and dual-phase nanocrystalline hard coatings. *Surf. Coat. Technol.* **2003**, *174–175*, 725–731. [[CrossRef](#)]
4. Lee, J.W.; Kuo, Y.C.; Wang, C.J.; Chang, L.C.; Liu, K.T. Effects of substrate bias frequencies on the characteristics of chromium nitride coatings deposited by pulsed DC reactive magnetron sputtering. *Surf. Coat. Technol.* **2008**, *203*, 721–725. [[CrossRef](#)]
5. Shan, L.; Wang, Y.; Li, J.; Jiang, X.; Chen, J. Improving tribological performance of CrN coatings in seawater by structure design. *Tribol. Int.* **2015**, *82*, 78–88. [[CrossRef](#)]
6. Liu, C.; Bi, Q.; Matthews, A. EIS comparison on corrosion performance of PVD TiN and CrN coated mild steel in 0.5 N NaCl aqueous solution. *Corros. Sci.* **2001**, *43*, 1953–1961. [[CrossRef](#)]
7. Navinšek, B.; Panjan, P. Oxidation resistance of PVD Cr, Cr–N and Cr–N–O hard coatings. *Surf. Coat. Technol.* **1993**, *59*, 244–248. [[CrossRef](#)]
8. Mayrhofer, P.H.; Willmann, H.; Mitterer, C. Oxidation kinetics of sputtered Cr–N hard coatings. *Surf. Coat. Technol.* **2001**, *146–147*, 222–228. [[CrossRef](#)]
9. Chen, H.Y.; Lu, F.H. Oxidation behavior of chromium nitride films. *Thin Solid Films* **2006**, *515*, 2179–2184. [[CrossRef](#)]
10. Meng, C.; Yang, L.; Wu, Y.; Tan, J.; Dang, W.; He, X.; Ma, X. Study of the oxidation behavior of CrN coating on Zr alloy in air. *J. Nucl. Mater.* **2019**, *515*, 354–369. [[CrossRef](#)]
11. Barshilia, H.C.; Selvakumar, N.; Deepthi, B.; Rajam, K.S. A comparative study of reactive direct current magnetron sputtered CrAlN and CrN coatings. *Surf. Coat. Technol.* **2006**, *201*, 2193–2201. [[CrossRef](#)]
12. Lin, J.; Mishra, B.; Moore, J.J.; Sproul, W.D. A study of the oxidation behavior of CrN and CrAlN thin films in air using DSC and TGA analyses. *Surf. Coat. Technol.* **2008**, *202*, 3272–3283. [[CrossRef](#)]
13. Martinez, E.; Sanjines, R.; Banakh, O.; Lévy, F. Electrical, optical and mechanical properties of sputtered CrN_y and Cr_{1-x}Si_xN_{1.02} thin films. *Thin Solid Films* **2004**, *447–448*, 332–336. [[CrossRef](#)]
14. Hones, P.; Consiglio, R.; Randall, N.; Lévy, F. Mechanical properties of hard chromium tungsten nitride coatings. *Surf. Coat. Technol.* **2000**, *125*, 179–184. [[CrossRef](#)]
15. Lin, C.H.; Duh, J.G.; Yau, B.S. Processing of chromium tungsten nitride hard coatings for glass molding. *Surf. Coat. Technol.* **2006**, *201*, 1316–1322. [[CrossRef](#)]
16. Kim, G.S.; Kim, B.S.; Lee, S.Y.; Hahn, J.H. Structure and mechanical properties of Cr–Zr–N films synthesized by closed field unbalanced magnetron sputtering with vertical magnetron sources. *Surf. Coat. Technol.* **2005**, *200*, 1669–1675. [[CrossRef](#)]
17. Park, J.H.; Chung, W.S.; Cho, Y.R.; Kim, K.H. Synthesis and mechanical properties of Cr–Si–N coatings deposited by a hybrid system of arc ion plating and sputtering techniques. *Surf. Coat. Technol.* **2004**, *188–189*, 425–430. [[CrossRef](#)]
18. Thobor-Keck, A.; Lapostolle, F.; Dehlinger, A.S.; Pilloud, D.; Pierson, J.F.; Coddet, C. Influence of silicon addition on the oxidation resistance of CrN coatings. *Surf. Coat. Technol.* **2005**, *200*, 264–268. [[CrossRef](#)]
19. Mercs, D.; Bonasso, N.; Naamane, S.; Bordes, J.M.; Coddet, C. Mechanical and tribological properties of Cr–N and Cr–Si–N coatings reactively sputter deposited. *Surf. Coat. Technol.* **2005**, *200*, 403–407. [[CrossRef](#)]

20. Lee, H.Y.; Jung, W.S.; Han, J.G.; Seo, S.M.; Kim, J.H.; Bae, Y.H. The synthesis of CrSiN film deposited using magnetron sputtering system. *Surf. Coat. Technol.* **2005**, *200*, 1026–1030. [[CrossRef](#)]
21. Sandu, C.S.; Sanjinés, R.; Benkahoul, M.; Medjani, F.; Lévy, F. Formation of composite ternary nitride thin films by magnetron sputtering co-deposition. *Surf. Coat. Technol.* **2006**, *201*, 4083–4089. [[CrossRef](#)]
22. Lee, J.W.; Chang, Y.C. A study on the microstructures and mechanical properties of pulsed DC reactive magnetron sputtered Cr–Si–N nanocomposite coatings. *Surf. Coat. Technol.* **2007**, *202*, 831–836. [[CrossRef](#)]
23. Benkahoul, M.; Robin, P.; Gujrathi, S.C.; Martinu, L.; Klemberg-Sapieha, J.E. Microstructure and mechanical properties of Cr–Si–N coatings prepared by pulsed reactive dual magnetron sputtering. *Surf. Coat. Technol.* **2008**, *202*, 3975–3980. [[CrossRef](#)]
24. Shin, S.H.; Kim, M.W.; Kang, M.C.; Kim, K.H.; Kim, K.H.; Kwon, D.H.; Kim, J.S. Cutting performance of CrN and Cr–Si–N coated end-mill deposited by hybrid coating system for ultra-high speed micro machining. *Surf. Coat. Technol.* **2008**, *202*, 5613–5616. [[CrossRef](#)]
25. Zhang, G.; Wang, L.; Wang, S.C.; Yan, P.; Xue, Q. Structure and mechanical properties of reactive sputtering CrSiN films. *Appl. Surf. Sci.* **2009**, *255*, 4425–4429. [[CrossRef](#)]
26. Lin, J.; Wang, B.; Ou, Y.; Sproul, W.D.; Dahan, I.; Moore, J.J. Structure and properties of CrSiN nanocomposite coatings deposited by hybrid modulated pulsed power and pulsed dc magnetron sputtering. *Surf. Coat. Technol.* **2013**, *216*, 251–258. [[CrossRef](#)]
27. Veprek, S.; Veprek-Heijman, M.G.J.; Karvankova, P.; Prochazka, J. Different approaches to superhard coatings and nanocomposites. *Thin Solid Films* **2005**, *476*, 1–29. [[CrossRef](#)]
28. Kim, K.H.; Choi, S.R.; Yoon, S.Y. Superhard Ti–Si–N coatings by a hybrid system of arc ion plating and sputtering techniques. *Surf. Coat. Technol.* **2002**, *298*, 243–248. [[CrossRef](#)]
29. Tien, S.K.; Duh, J.G.; Lee, J.W. Oxidation behavior of sputtered CrN/AlN multilayer coatings during heat treatment. *Surf. Coat. Technol.* **2007**, *201*, 5138–5142. [[CrossRef](#)]
30. Castaldi, L.; Kurapov, D.; Reiter, A.; Shklover, V.; Schwaller, P.; Patscheider, J. High temperature phase changes and oxidation behavior of Cr–Si–N coatings. *Surf. Coat. Technol.* **2007**, *202*, 781–785. [[CrossRef](#)]
31. Zhang, Z.G.; Rapaud, O.; Bonasso, N.; Mercks, D.; Dong, C.; Coddet, C. Control of microstructures and properties of dc magnetron sputtering deposited chromium nitride films. *Vacuum* **2008**, *82*, 501–509. [[CrossRef](#)]
32. Liu, S.C.; Chen, Y.I.; Tsai, H.Y.; Lin, K.C.; Chen, Y.H. Thermal stability of Ir–Re coatings annealed in oxygen-containing atmospheres. *Surf. Coat. Technol.* **2013**, *237*, 105–111. [[CrossRef](#)]
33. Chang, L.C.; Liu, B.W.; Chen, Y.I. Mechanical Properties and Oxidation Behavior of Multilayered Hf–Si–N Coatings. *Coatings* **2018**, *8*, 354. [[CrossRef](#)]
34. Oliver, W.C.; Pharr, G.M. An improved technique for determining hardness and elastic modulus using load and displacement sensing indentation experiments. *J. Mater. Res.* **1992**, *7*, 1564–1583. [[CrossRef](#)]
35. Olaya, J.J.; Wei, G.; Rodil, S.E.; Muhl, S.; Bhushan, B. Influence of the ion–atom flux ratio on the mechanical properties of chromium nitride thin films. *Vacuum* **2007**, *81*, 610–618. [[CrossRef](#)]
36. Janssen, G.C.A.M.; Abdalla, M.M.; van Keulen, F.; Pujada, B.R.; van Venrooy, B. Celebrating the 100th anniversary of the Stoney equation for film stress: Developments from polycrystalline steel strips to single crystal silicon wafers. *Thin Solid Films* **2009**, *517*, 1858–1867. [[CrossRef](#)]
37. Lee, J.W.; Tien, S.K.; Kuo, Y.C.; Chen, C.M. The mechanical properties evaluation of the CrN coatings deposited by the pulsed DC reactive magnetron sputtering. *Surf. Coat. Technol.* **2006**, *200*, 3330–3335. [[CrossRef](#)]
38. Čekada, M.; Panjan, P.; Navinšek, B.; Cvelbar, F. Characterization of (Cr,Ta)N hard coatings reactively sputtered at low temperature. *Vacuum* **1999**, *52*, 461–467. [[CrossRef](#)]
39. Choi, E.Y.; Kang, M.C.; Kwon, D.H.; Shin, D.W.; Kim, K.H. Comparative studies on microstructure and mechanical properties of CrN, Cr–C–N and Cr–Mo–N coatings. *J. Mater. Process. Technol.* **2007**, *187–188*, 566–570. [[CrossRef](#)]
40. Musil, J. Hard nanocomposite coatings: Thermal stability, oxidation resistance and toughness. *Surf. Coat. Technol.* **2012**, *207*, 50–65. [[CrossRef](#)]
41. Odén, M.; Ericsson, C.; Håkansson, G.; Ljungcrantz, H. Microstructure and mechanical behavior of arc-evaporated Cr–N coatings. *Surf. Coat. Technol.* **1999**, *114*, 39–51. [[CrossRef](#)]
42. Hones, P.; Diserens, M.; Lévy, F. Characterization of sputter-deposited chromium oxide thin films. *Surf. Coat. Technol.* **1999**, *120–121*, 277–283. [[CrossRef](#)]

43. Ji, A.L.; Wang, W.; Song, G.H.; Wang, Q.M.; Sun, C.; Wen, L.S. Microstructures and mechanical properties of chromium oxide films by arc ion plating. *Mater. Lett.* **2004**, *58*, 1993–1998. [[CrossRef](#)]
44. Eklund, P.; Sridharan, M.; Sillassen, M.; Böttiger, J. α -Cr₂O₃ template-texture effect on α -Al₂O₃ thin-film growth. *Thin Solid Films* **2008**, *516*, 7447–17450. [[CrossRef](#)]
45. Jeong, H.; Cho, J. Fabrication and evaluation of protective SiO_x layers using plasma-enhanced chemical vapor deposition. *Surf. Coat. Technol.* **2017**, *330*, 71–76. [[CrossRef](#)]



© 2019 by the authors. Licensee MDPI, Basel, Switzerland. This article is an open access article distributed under the terms and conditions of the Creative Commons Attribution (CC BY) license (<http://creativecommons.org/licenses/by/4.0/>).